PCCP

ROYAL SOCIETY OF CHEMISTRY

PAPER

View Article Online
View Journal

Check for updates

Cite this: DOI: 10.1039/d6cp00354k

Iron oxide nanoparticles by high-energy electron beam-assisted synthesis

Cezar Comanescu,[a] Gabriela Craciun,[b] Elena Manaila,[b] Cristian Radu,[a] Andrei Kuncser,[a] Petru Palade,[a] Victor Kuncser[a] and Nicusor Iacob *[a]

New approaches for the synthesis of magnetite (Fe_3O_4) nanoparticles (NPs) are of considerable interest due to their potential applications in various fields, such as biomedicine, industry, environmental remediation, and catalysis. This study presents a novel approach for synthesizing Fe_3O_4 NPs using high-energy electron beam (EB) irradiation starting from organic (acetylacetonates) iron precursors. EB irradiation is a challenging nanoparticle synthesis method, being at the same time efficient and rapid. The synthesis is carried out at room temperature and is based on the water radiolysis process. This eliminates the need for chemical-reducing agents and may provide precise control over particle formation. Using high-energy EB irradiation of an organic Fe precursor, we demonstrate the successful synthesis of well-dispersed Fe_3O_4 NPs with controlled size, morphology and magnetic properties, as proven by morpho-structural, Mössbauer spectroscopy and magnetic investigations. In particular, using organic iron precursors, such as iron acetylacetonates, NPs with distinct surface characteristics and improved thermal stability compared to those synthesized from inorganic precursors were obtained. These findings suggest that integrating organic precursors in EB-assisted synthesis can enhance the functional properties of Fe_3O_4 NPs, making them more suitable for specific applications. The versatility of this method opens up new avenues for the targeted design of nanomaterials with specific functionalities, paving the way for advanced applications in various technological fields. The current study is also motivated by the lack of literature data on the synthesis of metallic iron or iron oxide NPs mediated by EB radiolysis.

Received 30th January 2026,
Accepted 11th April 2026

DOI: 10.1039/d6cp00354k

rsc.li/pccp

Open Access Article. Published on 13 April 2026. Downloaded on 5/4/2026 9:53:30 PM.
This article is licensed under a Creative Commons Attribution-NonCommercial 3.0 Unported Licence.

1. Introduction

Fe_3O_4 nanoparticles (NPs) have attracted sustained interest owing to their favorable magnetic characteristics – high magnetic moment and saturation magnetization coupled with relatively low coercivity – and good biocompatibility. These properties underpin a broad spectrum of biomedical applications, including targeted drug delivery,[1,2] magnetic resonance imaging (MRI) contrast enhancement,[3,4] magnetic fluid hyperthermia,[5–7] and biosensing.[8,9] Additional uses span industrial processes,[10,11] biocatalysis,[12,13] and environmental remediation.[14]

Synthesis strategies have focused on precise control of particle size, morphology, crystallinity, and surface chemistry. A variety of chemical routes have been established, each with distinct advantages and limitations,[15] including (a) pyrolysis, (b) sol–gel, (c) co-precipitation, (d) thermal decomposition, and (e) hydrothermal methods, among others. Beyond these conventional chemistries, non-ionizing radiation-assisted synthesis (*e.g.*, microwaves[16,17] and ultrasound[18]) and ionizing-radiation approaches (γ-rays or electron beams (EBs)[19–21]) have been explored. The latter rely on water radiolysis – a cascade of ionization, excitation, dissociation, and recombination events triggered by energy deposition in aqueous media – thereby generating a chemically active environment rich in short-lived reactive species according to the global scheme (reaction (1)):[22–27]

$$H_2O \rightsquigarrow HO^\bullet + e_{aq}^- + H^\bullet + \{H_2 + H_2O_2 + H_3O^+\} \quad (1)$$

During radiolysis, numerous elementary reactions occur.[28–30] Of particular synthetic value are solvated electrons (e_{aq}^-) and hydrogen atoms ($H^\bullet$), which possess highly negative reduction potentials ($E_0(H_2O/e_{aq}^-) = -2.87$ V; $E_0(H^+/H^\bullet) = -2.3$ V), enabling the replacement of conventional, often non-eco-friendly reductants. Concurrently, oxidizing transients such as hydroxyl radicals ($^\bullet OH$) are formed but can be efficiently scavenged by alcohols (*e.g.*, 2-propanol (IPA)).

[a] National Institute of Materials Physics, 405 Atomistilor Street, Magurele, Ilfov, Romania
[b] National Institute for Lasers, Plasma and Radiation Physics, 409 Atomistilor Street, Magurele, Ilfov, Romania

Open Access Article. Published on 13 April 2026. Downloaded on 5/4/2026 9:53:30 PM.
This article is licensed under a Creative Commons Attribution-NonCommercial 3.0 Unported Licence.

Given the reactivity and the oxidation reactions of the $HO^{\bullet}$ radical, it may favor certain reaction pathways. The usage of IPA may further scavenge $HO^{\bullet}$ and $H^{\bullet}$ according to eqn (2) and (3) which are H-abstraction reactions:

$$HO^{\bullet} + (CH_3)_2CHOH \rightarrow H_2O + (CH_3)_2(C^{\bullet})OH \quad (2)$$

$$H^{\bullet} + (CH_3)_2CHOH \rightarrow H_2 + (CH_3)_2(C^{\bullet})OH \quad (3)$$

Formation of the α-alcohol radical $(CH_3)(C^{\bullet})OH$ rather than the β-alcohol radical $(^{\bullet}CH_2)(CH_3)(CH)OH$ is supported by several studies, where H-abstraction reactions from the α-carbon occur with yields in the range of 85.5–96%.[23] The remainder, up to 100%, are HO abstraction (1.2%) and β-carbon hydrogen abstraction reactions (13.3%).[23] The resulting $(CH_3)_2(C^{\bullet})OH$ radical remains, however, the major product and exhibits a strong reducing character. P. Wardman describes the reaction of hydroxyl radical $HO^{\bullet}$ with tertiary alcohols like *tert*-butanol $(CH_3)_3COH$, secondary alcohols like IPA $(CH_3)_2CHOH$, and formate (HCO_2^-).[24]

A further advantage of radiochemical synthesis is its operation near ambient temperature and pressure. Uniform nucleation is essential for obtaining monodisperse, colloidally stable NPs. Ionizing radiation can deliver spatially homogeneous energy deposition throughout the reaction volume when the irradiation geometry is appropriately configured. Consequently, accurate dosimetry and optimal irradiation-cell design are critical for controlling nucleation and growth kinetics.[31]

Cobalt-60 γ-sources are the most frequently employed ionizing sources for radiolytic nanoparticle synthesis.[32–34] γ-irradiation enables access to diverse nanoarchitectures, from single-phase materials[35,36] to multiphase systems – including alloy-like structures[37,38] and bi-/multi-metallic core–shell NPs.[39] In addition to standard synthetic variables (solvent, surfactant, and pH), the absorbed dose is a key handle for tailoring composition and structure. For iron-containing systems, the dose can modulate the Fe^{2+}/Fe^{3+} ratio[40] and thereby direct phase selection (*e.g.*, Fe_3O_4 *vs.* other iron oxides such as α-FeOOH), consistent with the proposed γ-induced nucleation-growth mechanisms for iron-oxide formation.[41]

High-energy electron beams represent an alternative ionizing source for radiolysis-based synthesis of metallic NPs.[42–44] EB irradiation offers high dose rates, short processing times, room-temperature operation, and fine, real-time tunability of the dose rate *via* pulse current, repetition frequency, irradiation geometry, and exposure time. For magnetic systems, EB-driven syntheses have demonstrated dose-dependent improvements in magnetic properties, as reported for Ni-based NPs up to ~300 kGy.[45] Although EB facilities are less ubiquitous than γ-sources, EB irradiation is increasingly utilized in radiolytic syntheses,[28,46] and modern accelerators also enable highly homogeneous volumetric irradiation and precise pulse-frequency control for dose-rate adjustment.[47]

Under pulsed ionizing irradiation, chemistry proceeds in two coupled regimes: (i) radiolysis during the pulse (typically microseconds for industrial EB sources) and (ii) interpulse evolution (milliseconds), wherein the system can be chemically "quiescent" (NPs largely unchanged) or reactive (solvent, alcohols, and surfactants interact with nascent clusters). These regimes can overlap kinetically, rendering EB-assisted radiolysis a versatile, highly tunable platform. *In situ* transmission electron microscopy (TEM) has provided valuable real-time insight into EB-induced radiolysis at hundreds of keV.[49,50]

Despite these advantages, EB-driven radiolytic synthesis of iron-oxide magnetic nanoparticles (MNPs) has only been reported very recently by Dietrich *et al.*,[22] who synthesized Fe_3O_4/maghemite from the $FeCl_3.6H_2O$ inorganic precursor *via* a microemulsion process involving the use of a surfactant (Triton X-100), toxic organic solvents (such as cyclohexane) and tetramethylammonium hydroxide (TMAH) as a precipitation reagent. However, we demonstrate herein the EB-radiolysis synthesis of Fe_3O_4 NPs from organic iron precursors (acetylacetonates) without the use of organic solvents and typical precipitation agents (such as NaOH) and provide comprehensive morpho-structural and magnetic characterization of the resulting materials.

2. Experimental

Iron-oxide nanoparticles (NPs) were synthesized radiolytically using 5.5 MeV EB pulses for 4 μs at a 50 Hz repetition rate[47,48] delivered by a linear electron accelerator ALID-7 at the National Institute for Laser, Plasma and Radiation Physics (Romania) (see Fig. S1 in the SI). Two independent attempts were performed employing $Fe(acac)_3$ as the Fe(III) precursor in IPA with 1 M NaOH in deionized and degassed water, while varying the EB dose rate. Iron(III) acetylacetonate precursors can facilitate control over the particle morphology and surface chemistry owing to their coordination environment and thermal decomposition characteristics.[51] The chemical substances were purchased from Sigma Aldrich and used as received.

The first attempt involved 0.15 g of the $Fe(acac)_3$ precursor dissolved in 5 mL of distilled water under vigorous stirring for 30 minutes, under the addition of 0.85 mL of NaOH 1 M and 0.2 mL of IPA, to neutralize the oxidative species. The precursor solution was placed in a small glass under the accelerator irradiation window for irradiation along with other samples which are not of interest for the present discussion. All samples were arranged on a circular area corresponding to the EB radiation footprint recorded on a borosilicate glass slide. The radiation dose rate during the experiment was 5 kGy min^{-1}, measured using a graphite calorimeter.[47,48]

Continuous irradiation at 5 kGy min^{-1} for 60 min delivered a total dose of 300 kGy. The resulting solid was magnetically separated and washed repeatedly with distilled water (IONP-300 kGy sample).

In the second attempt, the precursor loadings were adjusted to increase the nanoparticle yield. Specifically, 0.75 g of $Fe(acac)_3$ was dissolved in 25 mL of distilled water under vigorous stirring, followed by the addition of 4.25 mL of 1 M NaOH and 1.0 mL of IPA. The reaction mixture was transferred to a polyethylene vessel forming a 25 mm-thick liquid layer to

 This journal is © the Owner Societies 2026

Open Access Article. Published on 13 April 2026. Downloaded on 5/4/2026 9:53:30 PM.
This article is licensed under a Creative Commons Attribution-NonCommercial 3.0 Unported Licence.

enhance dose uniformity during irradiation; this thickness matches the depth-dose profile of a 5.5 MeV electron beam in water. The irradiation was performed at a dose rate of 8 kGy min^{-1} for 50 min to a total absorbed dose of 400 kGy. After irradiation, the resulting black suspension was collected by magnetic separation, washed several times with distilled water, and finally redispersed in absolute ethanol (IONP-400 kGy sample).

Morphology and structure of both samples were examined by transmission electron microscopy (TEM) and selected-area electron diffraction (SAED) on a JEM-ARM200F (JEOL) instrument. X-ray diffraction (XRD) patterns were collected in θ–2θ geometry on a Bruker D8 Advance diffractometer, and Rietveld refinements were carried out using MAUD.[52] Magnetic properties were measured using a SQUID magnetometer (MPMS, Quantum Design, USA) operating under the Reciprocating Sample Option (RSO) for enhanced sensitivity. ^{57}Fe Mössbauer spectra were acquired using a constant-acceleration spectrometer (SEECo, USA) with a symmetric waveform. Low-temperature measurements employed a helium closed-cycle Mössbauer cryostat (Janis, USA) mounted on a vibration-isolated table to minimize mechanical noise at the sample holder. Spectra were fitted with NORMOS,[53] and isomer shifts are reported relative to α-Fe at room temperature.

3. Results and discussion

3.1. XRD

According to the X-ray diffraction pattern, both samples contain Fe_3O_4 with a cubic structure (Fig. 1). Hematite could not be detected in the spectrum.

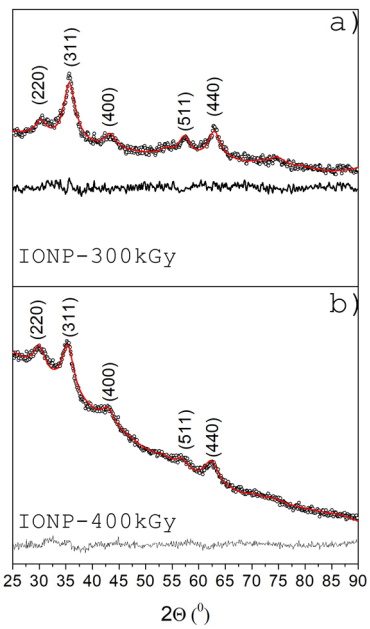

Fig. 1 XRD spectra recorded on samples IONP-300 kGy (a) and IONP-400 kGy (b) synthesized using the radiolytic route from the $Fe(acac)_3$ precursor solution irradiated with 5.5 MeV EB for 60 min at 5 kGy min^{-1} and for 50 min at 8 kGy min^{-1}, respectively.

The Rietveld refinements for sample IONP-300 kGy revealed a Fe_3O_4 lattice constant of 0.835(2) nm and a crystal size of 4.3(2) nm. The fit reliability parameters were goodness of fit (χ^2) of 1.14 and weighted profile factor, R_{wp}, after background extraction of 3.98%.

Similar, for sample IONP-400 kGy, the Fe_3O_4 lattice constant was 0.842(2) nm and the crystal size was 4.8(3) nm. The goodness of fit (χ^2) was 1.56 and the weighted profile factor, R_{wp}, after background extraction was 3.93%.

Additionally, in the SI (Fig. S2) are shown the XRD peak positions of different iron oxides and oxyhydroxides that could be theoretically generated in radiolysis synthesis, but do not appear in the measured XRD spectra of IONP-300 kGy and IONP-400 kGy samples. Accordingly, the presence of hematite and wustite can be excluded due to their highest intensity peaks at 2θ of 33.15° and 41.7°, respectively, which do not appear in the experimental pattern. The XRD patterns of iron oxyhydroxides or hydroxides reported in the ICDD database show high intensity peaks located in the 2θ range of 20–27° while the experimental spectra do not indicate any peaks in this region. Only magnetite and cubic maghemite which have a very similar XRD pattern fit well the experimental data.

3.2. TEM and SAED

TEM analysis revealed the presence of Fe_3O_4/γ-Fe_2O_3 nanoparticles (NPs) with an average diameter below 10 nm for both samples (Fig. 2a, b and 3a, b). Selected-area electron diffraction (SAED) displayed continuous diffraction rings without distinct high-intensity spots, indicating the presence of small, uniformly sized nanoparticles. In the case of IONP-300 kGy, a

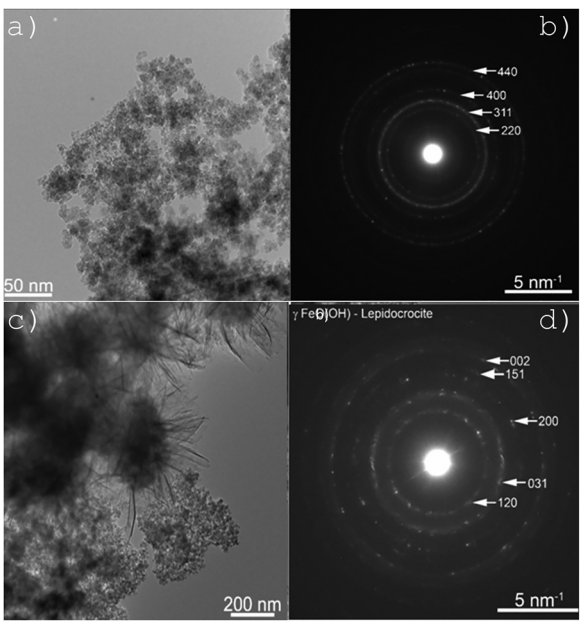

Fig. 2 TEM images and SAED patterns for sample IONP-300 kGy synthesized using the radiolytic route from $Fe(acac)_3$ precursor solution irradiated with 5.5 MeV EB for 60 minutes at 5 kGy min^{-1} revealed the Fe_3O_4/γ-Fe_2O_3 phase (a and b). The lepidocrocite phase is evidenced by SAED in a secondary morphology showing thin sheets and wires (c and d).

Open Access Article. Published on 13 April 2026. Downloaded on 5/4/2026 9:53:30 PM.
This article is licensed under a Creative Commons Attribution-NonCommercial 3.0 Unported Licence.

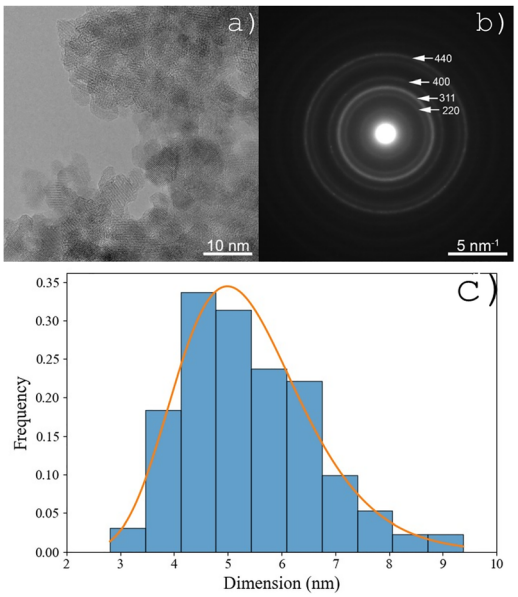

Fig. 3 TEM images (a), SAED patterns (b) and size distribution (c) of sample IONP-400 kGy synthesized using the radiolytic route from $Fe(acac)_3$ precursor solution irradiated with 5.5 MeV EB for 50 minutes at 8 kGy min^{-1} evidenced the Fe_3O_4/γ-Fe_2O_3 phase.

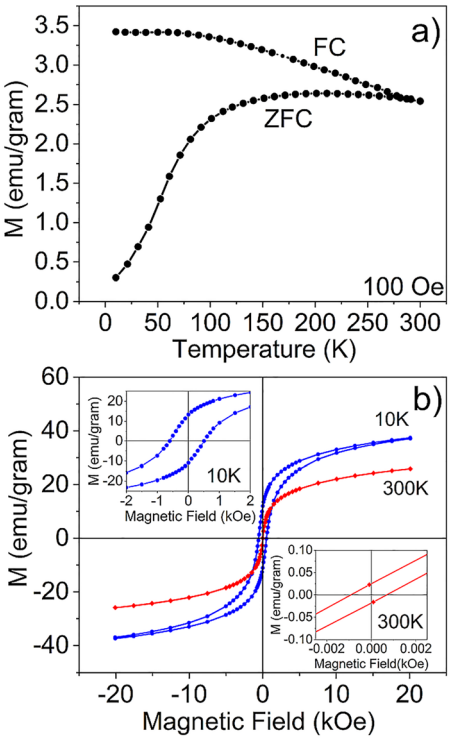

Fig. 4 The ZFC–FC curves measured under 100 Oe (a) and hysteresis loops measured at 10 K and 300 K (with a better field resolution shown in the inset) (b) for the sample IONP-300 kGy obtained from $Fe(acac)_3$ as a result of the radiolytic synthesis under 5.5 MeV EB and 5 kGy min^{-1} for 60 minute irradiation time.

secondary morphology consisting of thin sheets and wire-like structures – likely formed by the rolling of these sheets – was observed and identified through electron diffraction as corresponding to the lepidocrocite phase (γ-FeO(OH)) (Fig. 2c and d).

In the sample IONP-400 kGy, the nanoparticles are organized in loosely associated clusters, exhibiting limited agglomeration, and no additional iron-based crystalline phases were detected. In consequence, for this sample, a size distribution of nanoparticles was computed, as shown in Fig. 3c.

3.3. Magnetic and Mössbauer measurements

In order to thoroughly understand the magnetic behavior of the sediments in correlation with their real phase composition, local structure and nanoparticle characteristics, standard magnetic measurements complemented by temperature-dependent Mössbauer spectroscopy measurements were performed. In addition to examining the magnetic properties of the samples, the study also yielded important data regarding the average size and size distribution of the nanoparticles. This information was derived from magnetic relaxation effects, interpreted within the framework of the Langevin theory,[54,55] as will be discussed subsequently.

Zero-field-cooled/field-cooled (ZFC–FC) under 100 Oe between 10 K and 300 K and hysteresis loop analyses were performed in order to prove both the specific dynamics and magnetic monodomain behavior of the nanoparticles. ZFC–FC curves recorded for sample IONP-300 kGy (Fig. 4a) exhibit features characteristic of magnetic monodomain nanoparticles with a broad size distribution and a wide range of blocking temperatures, as indicated by the broad and nearly flat maximum of the ZFC curve. Specifically, the ZFC magnetization initially increases with temperature at low values, followed by a quasi-saturation above approximately 120 K. Beyond 250 K, only a slight decrease in magnetization is observed, implying the persistence of relatively large nanoparticles whose blocking temperatures remain above room temperature (RT).

The measured magnetic response cannot be ascribed to the large acicular nanoparticles associated with the lepidocrocite secondary phase, since this phase is antiferromagnetic at low temperatures and becomes paramagnetic above RT, exhibiting negligible magnetic susceptibility. Therefore, the observed magnetic behavior is attributed exclusively to the iron oxide nanoparticles. Furthermore, the FC curve, obtained upon cooling in an applied field of 100 Oe, diverges rapidly from the ZFC curve at decreasing temperature, maintaining consistently higher magnetization values, which confirms the magnetic monodomain nature of the iron oxide NPs.

Hysteresis loops recorded at 10 K and 300 K for the IONP-300 kGy are presented in Fig. 4b. The incomplete magnetic saturation at high fields, even at low temperatures, is characteristic of systems exhibiting partially disordered surface spins and antiferromagnetic (AFM) coupling within the sample. Therefore, a reliable estimation of the saturation magnetization can only be achieved through the law of approach to saturation.[56,57] At 10 K, the law of approach was applied in the approximation of the $1/H$ linear dependence of magnetization over the values obtained only in high fields. Therefore, the value of saturation magnetization was estimated to be 41.8 emu g^{-1}

This journal is © the Owner Societies 2026

Open Access Article. Published on 13 April 2026. Downloaded on 5/4/2026 9:53:30 PM.
This article is licensed under a Creative Commons Attribution-NonCommercial 3.0 Unported Licence.

with an Adj. *R*-square of 0.995. This value corresponds to about 46% of the bulk Fe_3O_4 value and roughly 25% lower than that typically observed for Fe_3O_4/γ-Fe_2O_3 nanoparticles (NPs) with an average size of ~10 nm synthesized by conventional chemical routes.[58–60]

This reduced magnetization arises not only from a highly disordered spin structure at the nanoparticle surface – despite the reasonably good crystallinity confirmed by SAED – but also, and more significantly, from the presence of an antiferromagnetic secondary phase, whose contribution is roughly estimated by Mössbauer Spectroscopy measurements to be more than 10 wt %. At 10 K, the coercive field (H_c) reaches about 1100 Oe, which is 7–8 times higher than that commonly reported for γ-Fe_2O_3/Fe_3O_4 NPs obtained *via* standard chemical synthesis. Moreover, the hysteresis loop measured at 10 K after field cooling (FC) in 100 Oe displays a negative shift of approximately 100 Oe, indicative of exchange bias effects *via* unidirectional anisotropy.[59] Both enhanced coercivity and the loop shift provide clear evidence for the presence of unidirectional anisotropy, most likely induced by interfacial exchange interactions between the ferrimagnetic Fe_3O_4/γ-Fe_2O_3 nanoparticles and the larger γ-FeO(OH) particles exhibiting antiferromagnetic ordering.

At 300 K, the coercivity drastically decreases to about 1.5 Oe, reflecting a dominant superparamagnetic contribution from the Fe_3O_4/γ-Fe_2O_3 NPs at room temperature and the decoupling of their interfacial pinning from the antiferromagnetic phase.

In the case of IONP-400 kGy, the ZFC–FC magnetization curves (Fig. 5a) show a much clearly evidenced ZFC maximum around 100 K, which corresponds to the blocking temperature within the DC magnetometry time window (on the order of seconds). As expected, this value is lower than the blocking temperature obtained from Mössbauer spectroscopy (as will be shown further), owing to the much shorter characteristic time scale of the latter (order of 10^{-8} s).[57] The better evidenced maximum of the ZFC curve indicates a narrow distribution of blocking temperatures of the NPs formed in this sample. The branching temperature, where the ZFC and FC curves start to diverge, being only slightly higher than T_B, supports the existence of magnetic monodomain nanoparticles with weak interparticle interactions.[59]

A distinctive feature appears around 140 K, marked by a steep decrease in magnetization when the temperature exceeds 135 K. Since this temperature is more than 10 K above the Verwey transition in bulk Fe_3O_4,[59] and given that particle size reduction, external pressure, stress, or oxidation generally lower the Verwey temperature, this anomaly is most plausibly attributed to a small, abrupt increase in magnetocrystalline anisotropy above this point. Indeed, approximately 135 K corresponds to the isotropic point in Fe_3O_4,[61] where the first-order anisotropy constant K_1 changes sign. Consequently, a sudden increase in anisotropy induces a slight decrease in magnetic susceptibility, contrary to the expected sharp magnetization increase typically observed above the Verwey transition.[62] This particular behavior, which is absent in conventionally synthesized Fe_3O_4 nanoparticles, is likely associated with the unconventional electron-beam-assisted processing route employed in this work.

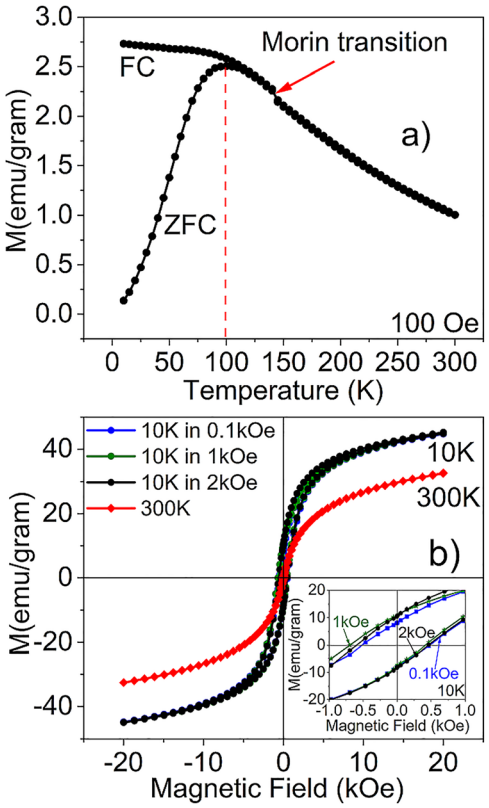

Fig. 5 The ZFC–FC curves measured under 100 Oe (a) and hysteresis loops measured at 10 K and 300 K (with a better field resolution shown in the inset) (b) for the sample IONP-400 kGy obtained from $Fe(acac)_3$ as a result of the radiolytic synthesis under 5.5 MeV EB and 8 kGy min^{-1} for 50 minute irradiation time.

Concerning the hysteresis loops recorded at 10 K and 300 K for IONP-400 kGy (Fig. 5b), they show a close behavior to that of IONP-300 kGy. Correspondingly, in the frame of the law of approach, the saturation magnetization at 10 K in $1/H$ approximation was estimated to be 50 emu g^{-1} value with an Adj. *R*-square of 0.9997, suggesting the presence of a tiny fraction of antiferromagnetic phase, most probable also of oxyhydroxide.

Careful examination of the TEM image shown in Fig. 3a reveals the formation of some small acicular structures, with average length smaller than 30 nm (*i.e.* much smaller than that in the case of IONP-300 kGy) giving a structural morphological proof for the presence of the α-FeOOH phase. However, this additional phase cannot be observed by diffraction methods due to the small structural coherence lengths. The coercive field is about 500 Oe at 10K and decreases to around 20 Oe at room temperature, both values being much closer to the ones specific to size-distributed Fe_3O_4 NPs as compared to the case of IONP-300 kGy.

This result provides additional proof for the fact that IONP-400 kGy contains a much larger amount of better formed Fe_3O_4 NPs as compared to the first experiment. A last proof for the presence of a minor fraction of antiferromagnetic nanoparticles was provided by the loops obtained after cooling down the system at 10 K under fields of 100, 1000 and 2000 Oe.

Open Access Article. Published on 13 April 2026. Downloaded on 5/4/2026 9:53:30 PM.
This article is licensed under a Creative Commons Attribution-NonCommercial 3.0 Unported Licence.

The loop obtained after cooling the sample under a field of 100 Oe at 10 K is characterized by an increased coercive field of 550 Oe as well as by an exchange bias field (negative shifts of the loops) of 140 Oe. These results show clearly the presence of unidirectional anisotropy also in this sample due to the interfacial interactions between the ferrimagnetic phase of Fe_3O_4 nanoparticles and the secondary antiferromagnetic phase. However, the related effects are much reduced, due to the lower amount and reduced size of antiferromagnetic NPs obtained for IONP-400 kGy compared to IONP-300 kGy.

Mössbauer spectra were recorded only for the IONP-400 kGy sample, which according to TEM and magnetic measurements consists predominantly of better-formed Fe_3O_4 nanoparticles. Several temperatures (6, 50, 100, 150, and 295 K) were considered in order to determine the iron phase composition within the magnetic sediment and to analyze the magnetic relaxation behavior of the sample (Fig. 6a). At 6 K, the spectrum exhibits a sextet profile with broadened absorption lines, typical of magnetic nanoparticles possessing distributed Fe environments and, consequently, a range of hyperfine parameters. Accordingly, the spectra were fitted using a distribution of magnetic hyperfine fields (B_{hf}), with the corresponding probability distributions shown to the right of each spectrum in Fig. 6b. Basically, a histogram of sextets with a linear change of isomer shifts is used. The relative areas of the sextet component are calculated using linear regression plus dumping.

The magnetic phase was identified based on the mean hyperfine parameters obtained at the lowest temperature (6 K). The magnetic relaxation processes were monitored through the temperature evolution of the B_{hf} distribution and its associated parameters.[11,58,59] As the temperature increases, the low-temperature magnetic sextet progressively collapses above 150 K into a dominant doublet component, accompanied by a shift of the main maximum in the B_{hf} distribution from approximately 51 T to below 10 T.

The hyperfine parameters derived from all recorded spectra – except for the spectrum at 295 K, where magnetic relaxation is completed – are summarized in Table 1. In this table, ⟨IS⟩ denotes the average isomer shift, ⟨QUA⟩ represents the average quadrupole splitting, $\langle B_{hf}(T)\rangle$ corresponds to the temperature-dependent mean magnetic hyperfine field, and B_{prob} indicates the most probable value of the magnetic hyperfine field.

According to Table 1, the mean isomer shift at the lowest investigated temperature (6 K) of 0.45 mm s^{-1} and the mean magnetic hyperfine field of 50.9 T are characteristic of defective γ-Fe_2O_3 and/or Fe_3O_4 phases.[11,58,59] Consequently, the analyzed sample is presumed to consist of fine magnetic nanoparticles with a defective spinel structure, ranging from predominantly Fe_3O_4-like to partially γ-Fe_2O_3-like configurations. A pronounced asymmetry is observed between the intensities of the first and sixth Mössbauer spectral lines, a feature typically associated with Fe_3O_4 above the Verwey transition temperature.[60] That means, the Verwey temperature is lower than 6 K for the present nanoparticles, supporting the different origin of the slight variation of magnetization in ZFC-FC curves at 140 K. Although, the 6 K Mössbauer spectrum does not support directly the presence of oxyhydroxide phases (their range of magnetic hyperfine fields can be framed under the distribution probability picked at about 51 T), a direct evidence of goethite (α-FeOOH) traces is provided by the 150 K Mössbauer spectrum. While the spectral contribution of iron oxide nanoparticles is almost relaxed, the still persisting local peaks in the hyperfine magnetic field distribution at 39 and 41 T give evidence of α-FeOOH magnetically unrelaxed nanoparticles which is the only oxyhydroxide phase with a magnetic order (*i.e.* antiferromagnetic) at this temperature. The relative area under the overall distribution, corresponding to the mentioned hyperfine magnetic fields, is about 10%, suggesting a similar relative amount of Fe ions which contribute to the antiferromagnetic phase. The mean quadrupole splitting exhibits a negligible value, indicative of a distributed configuration of Fe ions, as expected in this system.

The blocking temperature T_B within the Mössbauer time window can be defined from the temperature dependence of the magnetic hyperfine field distribution, as the temperature at which the mean magnetic hyperfine field decreases to half its maximum value,[58,59] corresponding to the transition from the blocked to the superparamagnetic regime. From Fig. 6b, the value of T_B = 122 K is obtained. The progressive and

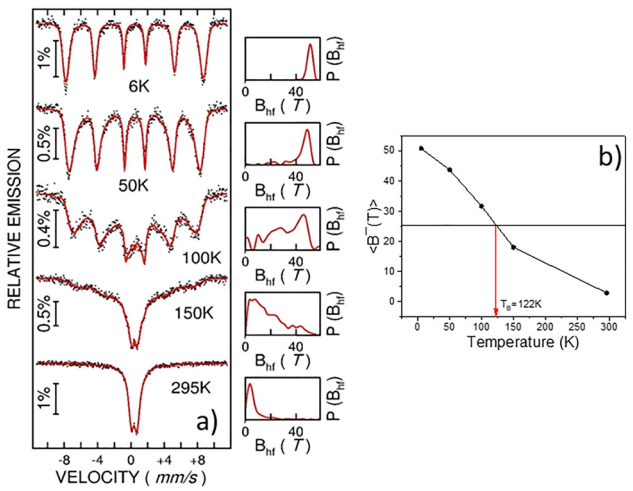

Fig. 6 Mössbauer spectra recorded at 6 K, 50 K, 100 K, 150 K and 295 K for the sample IONP-400 kGy obtained from $Fe(acac)_3$ precursor solution after EB irradiation at a 8 kGy min^{-1} dose rate for 50 minute irradiation time (a). The probability distributions of the magnetic hyperfine field are presented on the right-hand side of the corresponding spectra; the temperature evolution of the mean magnetic hyperfine field providing a blocking temperature of about 122 K for most of the magnetic NPs obtained (b).

Table 1 Hyperfine parameters of the IONP-400 kGy sample obtained and fitted *via* a distribution of magnetic hyperfine fields. The numbers in parentheses correspond to errors in the last-mentioned digit

Parameter	6 K	50 K	100 K	150 K
⟨IS (mm s^{-1})⟩	0.45(2)	0.45(2)	0.46(2)	0.44(2)
⟨QUA (mm s^{-1})⟩	−0.01(2)	−0.01(2)	−0.03(2)	−0.01(2)
B_{prob} (T)	51.0(2)	49.0(2)	Undefined	Undefined
$\langle B_{hf}$ (T)⟩	50.9(2)	43.8(2)	31.8(2)	18.1(2)

This journal is © the Owner Societies 2026

Open Access Article. Published on 13 April 2026. Downloaded on 5/4/2026 9:53:30 PM.
This article is licensed under a Creative Commons Attribution-NonCommercial 3.0 Unported Licence.

gradual decrease of $\langle B_{hf} \rangle$ with temperature suggests a distribution of blocking temperatures associated with Fe_3O_4 nanoparticles of various sizes, centered around 122 K. Nevertheless, a fraction of nanoparticles remains magnetically frozen even above 122 K, consistent with the presence of larger particles corresponding to a better-developed Fe_3O_4 phase.

Both Mössbauer spectroscopy and magnetic measurements can provide an estimation of the involved size of the magnetic NPs. A first route is to use the definition of the blocking temperature through the magnetic relaxation time.[59] Accordingly, the blocking temperature corresponds to that temperature where the relaxation time equates the time window of the used experimental technique, τ_M:

$$\tau_M = \tau_0 \exp(KV/kT_B) \quad (4)$$

where KV is the anisotropy energy of the NP, τ_0 is a time constant of the considered system and k is the Boltzmann constant. The most precise determination is obtained in the case of temperature-dependent Mössbauer spectroscopy investigation (the time window is precisely determined at 5×10^{-9} s) where T_B = 122 K. Assuming for the case of quasi-spherical magnetite NPs, a typical value of $K = 2 \times 10^4$ J m^{-3} and typical values for τ_0 in the range of 10^{-9} to 10^{-10} s, average particle sizes in the range from 5 to 7 nm are obtained. More imprecise results on the particle size would be obtained from the ZFC–FC evaluation of the blocking temperature, from the simple reason of the more imprecise estimation of the DC magnetometry time window (usually in the range from 1 to 100 s). However, the $M(H)$ data collected at a given temperature can be used better in this respect, thus avoiding the uncertainties related to the τ_0, τ_M and K values. Accordingly, the magnetization of the magnetite NP system, each nanoparticle carrying the magnetic moment μ, can be expressed as:

$$(H, T) = M_S L(x) + \chi_P \cdot H \quad (5)$$

where $L(x)$ is the Langevin function with $x = (\mu H/kT)$ and χ_P is a residual susceptibility responding to the combined effect of paramagnetic centers and field-induced change of noncollinear spin structure in the system.[54,55] The average magnetic moment of the nanoparticle can be expressed according to SI.

Both limits of the $L(x)$ functions, *i.e.* for $x \ll 1$ and $x \gg 1$, can be used for the estimation of the magnetic volume of the nanoparticles.[59] The condition $x \gg 1$ corresponding to the approximation $L(x) = 1$ is fulfilled for the measurements taken at the lowest temperature and in the highest fields. Accordingly, M_S and χ_P in eqn (2) were roughly estimated from the intersect and slope of the linear dependence in high fields of the $M(H)$ curve collected at 10 K. Values in the range of 30–35 emu g^{-1} and 0.0002–0.0004 emu g^{-1} Oe^{-1}, respectively, were estimated, depending on the highest field values considered.

In the next step, the $M(H)$ curve collected at 300 K and renormalized by a factor of 1.1 for disregarding the influence of the antiferromagnetic phase was considered for the evaluation of the nanoparticle size due to both the minimal influence of the residual susceptibility and negligible coercive fields.

The case of $x \ll 1$, leading to $L(x) = x/3$, corresponds to the linear variation of magnetization in low applied magnetic fields, according to the equation:

$$M(H) = (288 \cdot V \cdot M_S/3 \cdot k \cdot T) \cdot H + \chi_P \cdot H \quad (6)$$

The dependence of the experimental magnetization *versus* the field in the range of low fields, estimated for different nanoparticle sizes are shown in Fig. 7a (the plotted results are obtained for M_s = 33 emu g^{-1} and χ_p = 0.0003 emu g^{-1} Oe^{-1}, being quite insensitive to their variation in the previously mentioned range of values). The best fit of the experimental results is achieved for an average size of 6.1 nm for the magnetite nanoparticles, in close agreement with both TEM and Mössbauer estimations. The dependence of the experimentally derived $M(H)$ curve at 300 K over the full range of magnetic fields as well as the corresponding dependences for nanoparticle average sizes of 6.3 nm and 5.4 nm (slightly higher and slightly lower than 6.1 nm) is shown in Fig. 7b. This time the magnetization in high fields is very sensitive to the value of M_S, providing clearly the best convenient value of M_S = 33 emu g^{-1}. However, it can be observed that depending on the deviation from an average size, nanoparticles of smaller size give a better approximation of the experimental magnetization in high fields

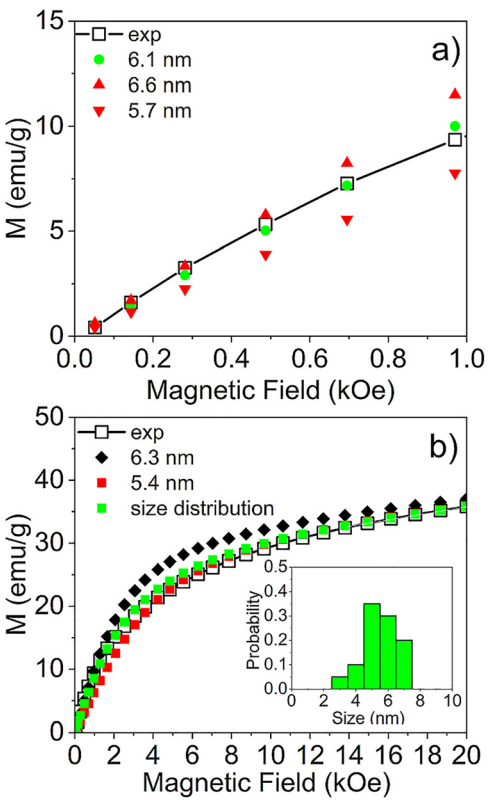

Fig. 7 Renormalized magnetization curve at 300 K in the range of low magnetic fields and simulated curves for different average sizes of magnetite nanoparticles (a) and renormalized magnetization curves over the whole range of magnetic fields and simulated curves for different average sizes as well as for distributed sizes (b); the distribution probability is shown in the inset.

Open Access Article. Published on 13 April 2026. Downloaded on 5/4/2026 9:53:30 PM.
This article is licensed under a Creative Commons Attribution-NonCommercial 3.0 Unported Licence.

whereas the ones of larger size give a better estimation of magnetization in low fields. Therefore, the best agreement with the experimental magnetization over the whole range of magnetic fields was obtained *via* the size distribution presented in the inset of Fig. 7b.

4. Conclusions

The obtained results demonstrate the versatility and effectiveness of electron-beam (EB) radiolytic synthesis for producing iron-based nanoparticles (NPs) from organic acetylacetonate precursors, without the need for chemical-reducing agents. Comprehensive morpho-structural, magnetic, and Mössbauer analyses confirmed the formation of well-dispersed, crystalline Fe_3O_4/γ-Fe_2O_3 nanoparticles as the main phase, accompanied by either γ-FeO(OH) or α-FeOOH as a secondary component. The relative content and crystallinity of the Fe_3O_4/γ-Fe_2O_3 phases can be significantly tuned by adjusting the processing parameters, with the irradiation dose exerting the most pronounced influence. Specific conditions – using $Fe(acac)_3$ as the precursor and EB irradiation at 5.5 MeV to a total dose of 400 kGy (8 kGy min^{-1}) – lead to magnetic nanoparticles with improved morpho-structural and magnetic characteristics. The average size of the nanoparticles as well as the size distribution evaluated by Mössbauer spectroscopy and magnetic measurements are in good agreement with the results obtained by TEM investigations. Interestingly, these EB-synthesized nanoparticles exhibit certain magnetic behaviors atypical of particles with similar size and morphology obtained *via* conventional chemical methods, warranting further fundamental investigation. Moreover, iron-based nanoparticles, particularly Fe_3O_4, possess broad technological applicability, providing strong motivation for continued exploration of this innovative EB-assisted route. The use of accelerated electrons to induce water radiolysis represents a promising, rapid, cost-effective, and environmentally friendly approach for large-scale nanoparticle synthesis. Overall, the findings highlight the potential for tailored fabrication of nanoparticles with customized properties for targeted applications. Future studies should assess the feasibility of employing alternative iron precursors in EB-assisted synthesis, paving the way for advanced applications in biomedicine, environmental remediation, and catalysis through the controlled design of magneto-functional nanomaterials.

Author contributions

Conceptualisation: C. Comanescu, N. Iacob, and G. Craciun; data curation: C. Radu, A. Kuncser, P. Palade, and V. Kuncser; formal analysis: G. Craciun and E. Manaila; methodology: C. Comanescu and N. Iacob; project administration: N. Iacob; supervision: N. Iacob and C. Comanescu; validation: A. Kuncser, V. Kuncser, G. Craciun, and E. Manaila; writing – original draft: C. Comanescu, V. Kuncser, and N. Iacob; writing – review and editing: C. Comanescu, G. Craciun, E. Manaila, C. Radu, A. Kuncser, P. Palade, V. Kuncser, and N. Iacob.

Conflicts of interest

There are no conflicts to declare.

Data availability

The data supporting the findings of this study are available from the corresponding author upon reasonable request.

The supplementary information contains additional details about the experimental setup, interpretation of XRD results and the estimation of the magnetic moment of the nanoparticle. See DOI: https://doi.org/10.1039/d6cp00354k.

Acknowledgements

This work is funded by the Core Program of the National Institute of Materials Physics, granted by the Romanian Ministry of Research, Innovation and Digitalization through Project PC1-PN23080101.

References

1 A. Pusta, M. Tertis, I. Crăciunescu and C. Cristea, *Pharmaceutics*, 2023, **15**, 1872.
2 M. J. Mitchell, M. M. Billingsley, R. M. Haley, M. E. Wechsler, N. A. Peppas and R. Langer, *Nat. Rev. Drug Discovery*, 2021, **20**(2), 101–124.
3 R. Lapusan, R. Borlan and M. Focsan, *Nanoscale Adv.*, 2024, **6**, 2234.
4 A. Avasthi, C. Caro and E. Pozo-Torres, *Top. Curr. Chem.*, 2020, **378**, 40.
5 A. Włodarczyk, S. Gorgon, A. Radon and K. Bajdak-Rusinek, *Nanomaterials*, 2022, **12**, 1807.
6 N. Iacob, A. Kuncser, C. Comanescu, P. Palade and V. Kuncser, *J. Nanopart. Res.*, 2020, **22**, 138.
7 N. Iacob, G. Schinteie, C. Bartha, P. Palade, L. Vekas and V. Kuncser, *J. Phys. D: Appl. Phys.*, 2016, **49**, 295001.
8 H. Khosravi, O. Carreras-Gallo and J. Casals-Terré, *Biosensors*, 2023, **13**, 957.
9 N. Dudchenko, S. Pawar, I. Perelshtein and D. Fixler, *Biosensors*, 2023, **13**, 304.
10 K. Zhou, X. Zhou, J. Liu and Z. Huang, *J. Pet. Eng.*, 2020, **188**, 106943.
11 G. Schinteie, P. Palade, L. Vekas, N. Iacob, C. Bartha and V. Kuncser, *J. Phys. D: Appl. Phys.*, 2013, **46**, 395501.
12 M. Bilal, E. U. Rashid, J. Zdarta, J. C. S. dos Santos, P. C. B. Fernandes, H. Cheng and T. J. Bilal, *Sustainable Chem. Pharm.*, 2022, **30**, 100866.
13 M. Seenuvasan, G. Vinodhini, C. G. Malar, N. Balaji and K. S. K. Seenuvasan, *IET Nanobiotechnol.*, 2018, **12**(5), 535–548.
14 M. M. Woldeamanuel, S. Mohapatra, S. Senapati, T. K. Bastia, A. K. Panda and P. Rath, Iron Oxide-Based Nanocomposites and Nanoenzymes, in *Nanostructure Science and Technology*, ed. H. Sahoo and J. K. Sahoo, Springer, Cham, 2024.

 This journal is © the Owner Societies 2026

Open Access Article. Published on 13 April 2026. Downloaded on 5/4/2026 9:53:30 PM. This article is licensed under a Creative Commons Attribution-NonCommercial 3.0 Unported Licence.

15 A. Ali, T. Shah, R. Ullah, P. Zhou, M. Guo, M. Ovais, Z. Tan and Y. R. Arbab, *Front. Chem.*, 2021, **9**, 629054.
16 T. Girardet, L. Verel, C. Dji, S. Bouguet-Bonnet, F. Cleymand and S. F. Girardet, *Pure Appl. Chem.*, 2022, **94**(10), 1149–1159.
17 L. Panariello, M. O. Besenhard, S. Damilos, A. Sergides, V. Sebastian, S. Irusta, J. Tang, N. T. K. Thanh and A. G. Panariello, *Chem. Eng. Process.*, 2022, **182**, 109198.
18 J. A. Fuentes-García, A. C. Alavarse, A. C. M. Maldonado, A. Toro-Cordova, M. R. Ibarra and G. F. Goya, *ACS Omega*, 2020, **5**, 26357–26364.
19 K. Čubová and V. Čuba, *Radiat. Phys. Chem.*, 2020, **169**, 108774.
20 J. Grand, S. R. Ferreira, V. de Waele, S. Mintova and T. M. Nenoff, *J. Phys. Chem. C*, 2018, **122**, 12573–12588.
21 D. M. Clifford, C. E. Castano and J. V. Rojas, *Radiat. Phys. Chem.*, 2017, **132**, 52–64.
22 J. Dietrich, V. Wolfer, R. Konieczny, A. Lotnyk, A. Kahnt and S. G. Mayr, *J. Phys. Chem. C*, 2024, **128**(40), 17013.
23 K. D. Asmus, H. Moeckel and A. Henglein, *J. Phys. Chem.*, 1973, **77**(10), 1218–1221.
24 P. Wardman, *J. Phys. Chem. Ref. Data*, 1989, **18**, 1637–1755.
25 K. P. Madden and S. P. Mezyk, *J. Phys. Chem. Ref. Data*, 2011, **40**, 023103.
26 B. H. J. Bielski, D. E. Cabelli, R. L. Arudi and A. B. Ross, *J. Phys. Chem. Ref. Data*, 1985, **14**, 1041.
27 G. V. Buxton, C. L. Greenstock, W. P. Helman and A. B. Ross, *J. Phys. Chem. Ref. Data*, 1988, **17**, 513–886.
28 M. Siwek and T. Edgecock, *Environ. Sci. Pollut. Res.*, 2020, **27**, 42424–42448.
29 G. Craciun, E. Manaila and D. Ighigeanu, *Polymers*, 2019, **11**, 234.
30 G. Craciun, E. Manaila, M. Niculescu and D. Ighigeanu, *Polym. Bull.*, 2017, **74**, 1299–1326.
31 A. Abedini, A. R. Daud, M. A. A. Hamid, N. K. Othman and E. Saion, *Nanoscale Res. Lett.*, 2013, **8**, 474.
32 Y. Yang, M. Johansson, A. Wiorek, N. V. Tarakina, F. Sayed, R. Mathieu and M. Jonsson, *Dalton Trans.*, 2021, **50**, 376–383.
33 G. G. Flores-Rojas, F. López-Saucedo and E. Bucio, *Radiat. Phys. Chem.*, 2020, **169**, 107962.
34 L. M. Alrehaily, J. M. Joseph and J. C. Wren, *Phys. Chem. Chem. Phys.*, 2015, **17**, 2413.
35 I. V. Korolkov, O. Güven, O. Mashentseva, A. A. Atıcı, A. B. Gorin, Y. G. Zdorovets and M. V. Taltenov, *Radiat. Phys. Chem.*, 2017, **130**, 480–487.
36 E. Gharibshahi, E. Saion, A. Ashraf and L. Gharibshahi, *Appl. Radiat. Isot.*, 2017, **130**, 211–217.
37 A. Abedini, E. Saion, F. Larki, A. Zakaria, M. Noroozi and N. Soltani, *Int. J. Mol. Sci.*, 2012, **13**, 11941–11953.
38 J. Belloni, M. Mostafavi, H. Remita, J.-L. Marignier and M.-O. Delcourt, *New J. Chem.*, 1998, **22**, 1239–1255.
39 J. Belloni, *Catal. Today*, 2006, **113**, 141–156.
40 A. Abedini, A. R. Daud, M. A. Abdul Hamid and N. Kamil Othman, *PLoS One*, 2014, **9**(3), e90055.
41 T. I. Sutherland, C. J. Sparks, J. M. Joseph, Z. Wang, G. Whitaker, T. K. Sham and J. C. Wren, *Phys. Chem. Chem. Phys.*, 2017, **19**, 695.
42 B. Zhao, Y. Wang, H. Guo, J. Wang, Y. He, Z. JIao and M. Wu, *Mater. Sci.-Pol.*, 2007, **25**(4), 1143.
43 M. A. Laurenzi III, W.-A. Chiou and I. L. Pegg, *Microsc. Microanal.*, 2008, **14**(2), 442–443.
44 I. Calinescu, D. Martin, D. Ighigeanu, A. I. Gavrila, A. Trifan, M. Patrascu, C. Munteanu, A. Diacon, E. Manaila and G. Craciun, *Cent. Eur. J. Chem.*, 2014, **12**(7), 774–781.
45 S. J. Lee, H. B. Kim, S. H. Oh and P. H. Kang, *J. Magn.*, 2015, **20**(3), 241–245.
46 A. V. Ponomarev, *Radiat. Phys. Chem.*, 2020, **172**, 108812.
47 E. Manaila, G. Craciun, D. Ighigeanu, I. B. Lungu, M. Dumitru and M. D. Stelescu, *Polymers*, 2021, **13**, 1950.
48 G. Craciun, E. Manaila, D. Ighigeanu and M. D. Stelescu, *Polymers*, 2020, **12**, 215.
49 S. Pu, C. Gong and A. W. Robertson, *R. Soc. open sci.*, 2020, **7**, 191204.
50 J. Andrés, E. Longo, A. F. Gouveia, J. P. C. Costa, L. Gracia and M. C. Oliveira, *J. Mat. Sci. Eng.*, 2018, **7**, 3.
51 E. Scopel, P. P. Conti, D. G. S. Stroppa and C. J. Dalmaschio, *SN Appl. Sci.*, 2019, **1**, 147.
52 https://luttero.github.io/maud/.
53 https://wissel-instruments.de/index.php?option=com_content&task=view&id=6&Itemid=22.
54 Z. Nedelkoski, D. Kepaptsoglou, L. Lari, T. Wen, R. A. Booth, S. D. Oberdick, P. L. Galindo, Q. M. Ramasse, R. F. L. Evans, S. Majetich and V. K. Lazarov, *Sci. Rep.*, 2017, **7**, 45997.
55 M. Escoda-Torroella, C. Moya, A. F. Rodríguez, X. Batlle and A. Labarta, *Langmuir*, 2021, **37**, 35–45.
56 K. S. Sivaranjani, G. A. Jacob and R. J. Joseyphus, *Phys. Status Solidi B*, 2022, **259**, 2200050.
57 H. Zhang, D. Zeng and Z. Liu, *J. Magn. Magn. Mater.*, 2010, **322**, 2375–2380.
58 V. Kuncser, G. Schinteie, B. Sahoo, W. Keune, D. Bica, L. Vekas and G. Filoti, *J. Phys.: Condens. Matter*, 2007, **19**, 016205.
59 V. Kuncser, P. Palade, A. Kuncser, S. Greculeasa and G. Schinteie. *Size Effects in nanostructures: basics and applications*, 2017, pp. 169–237.
60 I. Craciunescu, P. Palade, N. Iacob, G. M. Ispas, A. E. Stanciu, V. Kuncser and R. P. Turcu, *J. Phys. Chem. C*, 2021, **125**, 11132–11146.
61 N. N. Greenwood and T. C. Gib, *Mössbauer Spectrsocopy*, Chapman and Hall Ltd, London, 1971.
62 H. Fuchs, A. Kontny and F. R. Schilling, *Geophys. J. Int.*, 2024, **238**(2), 794–805.